scientific reports

OPEN

Antimicrobial, photodegradation and BioReRAM applications of multifaceted green zinc oxide nanoparticles synthesized using coffee leaves extract

Vanessa de Oliveira Arnoldi Pellegrini[1], Aparecido de Jesus Bernardo[1], Bruno Roberto Rossi[2], Ramon Resende Leite[1], João Fernando Possatto[1], Andrei Nicoli Gebieluca Dabul[3], Carla Raquel Fontana[3], Zolile Wiseman Dlamini[4], Tebogo Sfiso Mahule[5], Belda Q. Mosepele[6], Force Tefo Thema[6]✉, Bhekie B. Mamba[7], Maria Ines Basso Bernardi[1], Sreedevi Vallabhapurapu[8], Vijaya Srinivasu Vallabhapurapu[5] & Igor Polikarpov[1]✉

The comprehensive utilization of plant biomass is a cornerstone in the development of sustainable circular bioeconomy. Several studies explore the conversion of primary biomass polymers and macromolecules, such as cellulose, hemicellulose, and lignin, into value-added chemical compounds, sustainable materials and biofuels. However, extractives warrant further investigations. Coffee, being one of the most consumed and produced global commodity and therefore widely available in a number of countries, presents an exciting study case. Here, we have employed fresh coffee leaves extract for the synthesis of zinc oxide nanoparticles (ZnO NPs). The synthesized ZnO NPs were characterized, including ultraviolet-visible and Fourier transform infrared spectroscopies, dynamic light scattering, scanning electron microscopy, X-ray diffraction, electron paramagnetic resonance, energy-dispersive X-ray spectroscopy, and thermal gravimetric analysis. Nanoscale size and reduced optical bandgap (3.2 eV) of the ZnO NPs contributed to their significant antimicrobial and photodegradation effects. Furthermore, with the aim of producing biological Resistive Random-Access Memory (bioReRAM) devices, we successfully explored the resistive switching properties of chitosan polysaccharide doped with the ZnO NPs.

Keywords ZnO nanoparticles, Green synthesis, Coffee leaves extract, Antimicrobial properties, Photodegradation effects, BioReRAMs

Holistic use of plant biomass is essential for the development of the sustainable circular bioeconomy[1]. A circular economy relies on the value of resources being maximized and implies that there is an imperative to recover and to valorize all waste- and side-streams. Plant biomass is highly significant for the circular economy both for production of materials and chemical compounds, manufacturing products and providing energy and fuels[2]. While pretreatments, enzymatic hydrolysis, fermentation and/or catalytic upgrading allows for conversion of main biomass polymers and macromolecules such as cellulose, hemicellulose and lignin into value-added

[1]São Carlos Institute of Physics, University of São Paulo, Avenida João Dagnone, 1100, Jardim Santa Angelina, São Carlos, SP CEP 13563-120, Brazil. [2]São Carlos Institute of Chemistry, University of São Paulo, Av. Trabalhador Sãocarlense, 400, São Carlos, SP 13566-590, Brazil. [3]School of Pharmaceutical Sciences, São Paulo State University, Rodovia Araraquara-Jaú, km 01, Araraquara, SP 14800-903, Brazil. [4]Maths, Science and Technology Education, Central University of Technology, 20 President Brand Street, Bloemfontein 9300, Free State, South Africa. [5]Physics Department, University of South Africa, 28 Pioneer Avenue, Florida Park, Johannesburg 1710, Gauteng, South Africa. [6]Botswana University of Agriculture and Natural Resources (BUAN), Private bag 0027, Gaborone, Botswana. [7]Institute for Nanotechnology and Water Sustainability, College of Science, Engineering and Technology, University of South Africa, Florida, Private Bag X6, Johannesburg 1709, Gauteng, South Africa. [8]School of Computing, University of South Africa, 28 Pioneer Avenue, Florida Park, Johannesburg 1710, Gauteng, South Africa. ✉email: ftthema@buan.ac.bw; ipolikarpov@ifsc.usp.br

chemical compounds, renewable materials and biofuels[3,4]. Primary plant biomass polymers (cellulose, hemicellulose, lignin) are commonly studied for conversion into value-added products, such as glucose, cellulosic ethanol, nanocellulose, prebiotics, oligosaccharides, nano-lignin, vanilin and other aromatic compounds, bulk chemicals and bioplastics, to name a few[5]. While primary plant biomass polymers are being used to generate biofuels, platform chemicals, resins, bioplastics, additives, and diversified biobased materials for a number of applications[6], extractives still remain insufficiently explored part of the plant biomass.

Optimum utilization of renewable lignocellulosic feedstocks should include recovery of value-added phytochemicals, thus reducing waste streams and increasing economic feasibility and sustainability of integrated biorefineries[7]. Plants contain significant amount of overlooked non-structural components (extractives), that include lipids (terpenes and terpenoids), waxes and fats, phenolic compounds (phenols, lignans, flavonoids and tannins), and alkaloids. The extractives have important chemical and biological properties[8] and can serve as precursors for bioactive compounds or green synthesis agents.

Coffee is one of the most relevant commodities in the world and one of the most popular drinks worldwide. This crop is grown by over 25 million farmers in more than 60 countries[9], with Brazil being the biggest coffee-producing country[10].

Recent studies have revealed that fresh coffee leaves extract contains a number of bioactive compounds, exhibiting promising antioxidant, anti-inflammatory, anticancer, antidiabetic, and analgesic properties, thereby positioning it as a potential therapeutic agent in the management and prevention of various health conditions[11,12]. Coffee leaves contain several phytochemicals such as alkaloids, flavonoids, terpenes, tannins, xanthonoids, phenolic acids, phytosterol, amino acids and carotenoids, which confer coffee its health beneficial properties[13,14]. Phytochemical compounds found in coffee leaves are known to act both as reducing and electrostatic stabilizing agents for bioengineered synthesis of metal oxide NPs[15].

One of the multiple ways to valorize plant extractives is via their use in green biosynthesis of metal and metal oxide nanoparticles (NPs). NPs frequently exhibit distinctive size-dependent features, differing significantly from those of bulk materials, mostly due to their tiny size and huge surface area. These particular physical characteristics lead to a wide range of novel applications in a wide range of areas such as the environment, agriculture, food, biotechnology and biomedicine, to name a few[16,17]. Due to the large surface-to-volume ratio, the NPs are endowed with unique physicochemical properties and biological activities[18,19].

NPs can be produced by a variety of physical and chemical processes. The strategy applied and the process variables such as temperature, time and compound concentration, among others have a significant impact on the morphology, stability, and physicochemical characteristics of the NPs[20]. Within recent years, green synthesis methods of NPs are gaining increasing attention. While the conventional NP synthesis is related to environmental pollution, large energy consumption, and potential health problems, the biological approaches arise as environmentally friendly alternatives[21,22]. Green NP synthesis is fully aligned with the objectives of the United Nations Sustainable Development Goals (UNSDGs), including clean water and sanitation (UNSDG6), responsible consumption and production (UNSDG12), climate action (UNSDG13), life below water (UNSDG14) and life on land (UNSDG15).

Different biogenic sources such as microorganisms, agro-waste and plant extracts have been used for the green synthesis of NPs[23]. The utilization of plant extracts stands out as a rather simple and easy process of NPs production in comparison, for example, to using microorganisms for NP growth. The latter process requires multiple steps such as isolation and culture development and maintenance, which add to its complexity. In general, technical and morphological properties of bioengineered zinc oxide (ZnO) NPs are like that of chemically or physically produced ZnO NPs, but green biosynthetic procedures are known to be more ecofriendly, simple, efficient, inexpensive and more suitable, for example, for biomedical applications[24] (Supplementary Table S1).

Green synthesis using plant extracts offers a huge diversity of the green biotechnological techniques of NPs synthesis, considering a wide diversity of available plants, shrubs, trees and grasses. Furthermore, the use of leaves, bark, and other agro-industrial residues is attractive for a sustainable development that meets the current demands for green production of nanomaterials. Although green synthesis methods based on plant extracts have several advantages, also have some challenges, particularly at an industrial scale. One of them is the availability of the plant source, and seasonal and regional variability of plant extract quantities and chemical composition which can lead to the variations in the NPs parameters and yields.

However, similar challenges are also encountered in other technologies involving plant extracts, such as traditional medicine, medicinal plant extracts utilization and the production of beverages and products based on plant extracts, such as, for example, tea and coffee. Therefore, there is a need for further exploring biogenic-based NPs synthesis approaches, particularly based on plant sources available on an industrial scale, such as coffee.

Potentially, industrial implementation of the bioengineered NPs production technologies can bring additional revenues to the coffee producers worldwide. Therefore, there is a need for further exploring biogenic-based NPs synthesis approaches, particularly based on agricultural plants available at an industrial scale, such as coffee.

Physical, chemical and morphological characteristics of NPs mainly depend on the types and species of plants used and the reaction conditions such as the pH, temperature, and synthesis media[25]. In the present study, we used fresh coffee leaves to synthesize ZnO NPs. ZnO NPs were chosen for this study due to their distinctive optical and chemical properties and a wide range of potential applications in biological sensing, gene transfer, biological labeling, medical implant coatings, electronic sensors, wastewater treatment, photocatalytic and antimicrobial activities[26]. ZnO NPs also demonstrate elevated photocatalytic and antibacterial activity against reactive dyes and bacterial strains. Photocatalytic degradation using ZnO NPs is an effective method to alleviate environmental impacts caused by organic pollutants[27], whereas their elevated antimicrobial activities are of particular importance for treating pathogenic bacterial multi resistant strains[28].

One of the promising areas for metal oxide NPs applications is Resistive Random-Access Memory (ReRAMs) manufacturing. Resistive switching memory is a new memory technology to store digital data based on different resistance states. A typical ReRAM device has a metal-insulator-metal (MIM) architecture consisting of a resistive switching material, known as the active layer, sandwiched between two electrodes. This device can have at least two electrically switchable resistive states, namely a low resistive state (LRS) and a high resistive state (HRS), which can be interpreted as logic 1 and 0, respectively in digital electronics language[29]. The HRS of a ReRAM device can be switched to a LRS during the set process, and back during the reset process, by applying a desired voltage pulse. ReRAMs are more scalable than conventional memory devices due to their simple construction, which does not require a driver transistor. Furthermore, ReRAMs exhibit quick programming speed, high endurance, and long-term data retention, allowing them to combine the advantages of dynamic random-access memory and flash memory in a single device. ReRAMs manufactured from inorganic materials, often known as inorganic ReRAMs, have advanced significantly in comparison to organic/bioReRAMs. As a result, a ReRAM prototype with 16 Gb capacity, 200 MB/s write, and 1 GB/s read speed was produced in 2009[30]. BioReRAMs have lately attracted interest due to their significantly lower environmental footprint and fascinating capabilities such as multilevel resistive switching, which allows more than one bit of data to be stored in a single cell. This synaptic-like feature may facilitate the creation of artificial synapses and other advanced electronic devices[31,32]. This work reports a first bioReRAM built using chitosan and green synthesized ZnO NPs. ZnO is a biodegradable material that has been widely used as an active layer in numerous ReRAM systems. Nowak et al. provide a detailed review that focuses solely on ZnO and ZnO materials for ReRAM devices[33]. Despite the fact that ZnO has been widely employed in ReRAM devices, there have been relatively few reports of ZnO being used as a dopant to produce a composite for ReRAM applications, and even less on ZnO and chitosan together. Chitosan, a biodegradable and abundant polymer, has been widely exploited as a polymer matrix in the construction of functional materials for ReRAM[29,34]. As a result, combining these two materials in present work assures that the bioReRAM has a low environmental footprint. In a related study, chemically-synthesized aluminium-doped ZnO (AlxZn(1-x)O) with chitosan was used to create a ReRAM consisting of indium-doped tin oxide (ITO) and titanium (Ti) electrodes[35]. AlxZn(1-x)O (with x = 0.03) demonstrated improved switching capabilities than undoped ZnO. The use of green synthesized ZnO in a chitosan composite is novel, as the entire active/functional switching layer is resourced from "green origins". Further it was already demonstrated that a record HRS/LRS ratio of 7 orders of magnitude, in the Chitosan-Al doped ZnO system and this is a motivation to choose chitosan as a host matrix for our green synthesized ZnO in this work. In addition, to emphasize green manufacturing, our device was built utilizing the drop cast method on the ITO layer and dried at room temperature without the use of power or heat and were able to obtain critical ReRAM device parameters.

In this work we biosynthesized ZnO NPs using coffee leaves extract. The synthesized NPs were characterized using ultraviolet-visible (UV-Vis) spectroscopy, Fourier transform infrared spectroscopy (FTIR), dynamic light scattering (DLS), scanning electron microscopy (SEM), energy-dispersive X-ray spectroscopy (EDS), X-ray diffraction (XRD), electron spin resonance (ESR) and thermal gravimetric analysis (TGA). We demonstrated antimicrobial characteristics of the ZnO NPs and evaluated their photodegradation potential. Furthermore, the resistive switching properties of the obtained ZnO NPs, which can be used for biological resistive switching random-access memory (bioReRAM) production were also investigated and successful construction of ZnO NP-chitosan based bioReRAM has been demonstrated for the first time.

Results and discussion

XRD analysis

XRD analysis was used to evaluate the biogenic ZnO NPs synthesized using coffee leaves extract. The well-defined strong diffraction peaks (Fig. 1), with 2θ values of 31.58°, 34.28°, 36.06°, 47.38°, 56.42°, 62.70°and 67.80° were observed. Those correspond to the crystallographic planes (100), (002), (101), (102), (110), (103), (112) of ZnO NPs, respectively, revealing that the sample has a polycrystalline hexagonal wurtzite structure (JCPDS 5-0664)[36]. No other secondary phase has been observed in the experimental XRD patterns (Fig. 1). Out of all existing ZnO NPs structures, the hexagonal wurtzite structure is the most stable one and this is potentially beneficial for photocatalytic and biomedical applications of the NPs[37].

The average crystallite size of ZnO NPs produced using coffee leaves extract was estimated using the Scherrer equation.

$$D = \frac{K\lambda}{\beta \cos\theta} \tag{1}$$

where D is the crystallite size, K Shape factor (K = 0.9), λ is the wavelength of X-rays used (1.5406 Å), θ is the angle of diffraction and β is full width on a half maximum of the diffraction peaks. The Scherrer equation assumes that the broadening of diffraction peaks is solely due to crystallite size, thus strain effects are ignored.

The average crystallite size of the synthesized ZnO NPs is in the nanoscale range and corresponds at 9.97 nm (Supplementary Table S2). The average crystallite size was reported to be affected by a number of process parameters, including pH of synthesis[38], amount of plant extract used for NP synthesis[39] and sintering temperature[40] to name a few. An average crystallite size determined in present work is in general agreement with the previous studies.

UV-Vis spectrophotometric measurements

It is known that ZnO NPs have characteristic absorption peaks between 310 and 380 nm due to their surface plasmonic resonance (SPR) band[41]. Figure 2 illustrates the UV-Vis absorption spectrum in the wavelength range of 220 to 850 nm. It is observed that the ZnO NPs exhibit intrinsic absorption in the ultraviolet region (λ < 400 nm) and low absorption in the visible region (λ > 400 nm). ZnO is a wide bandgap semiconductor, and the UV absorption is due to direct transitions between the valence band (primarily O 2p orbitals) and the

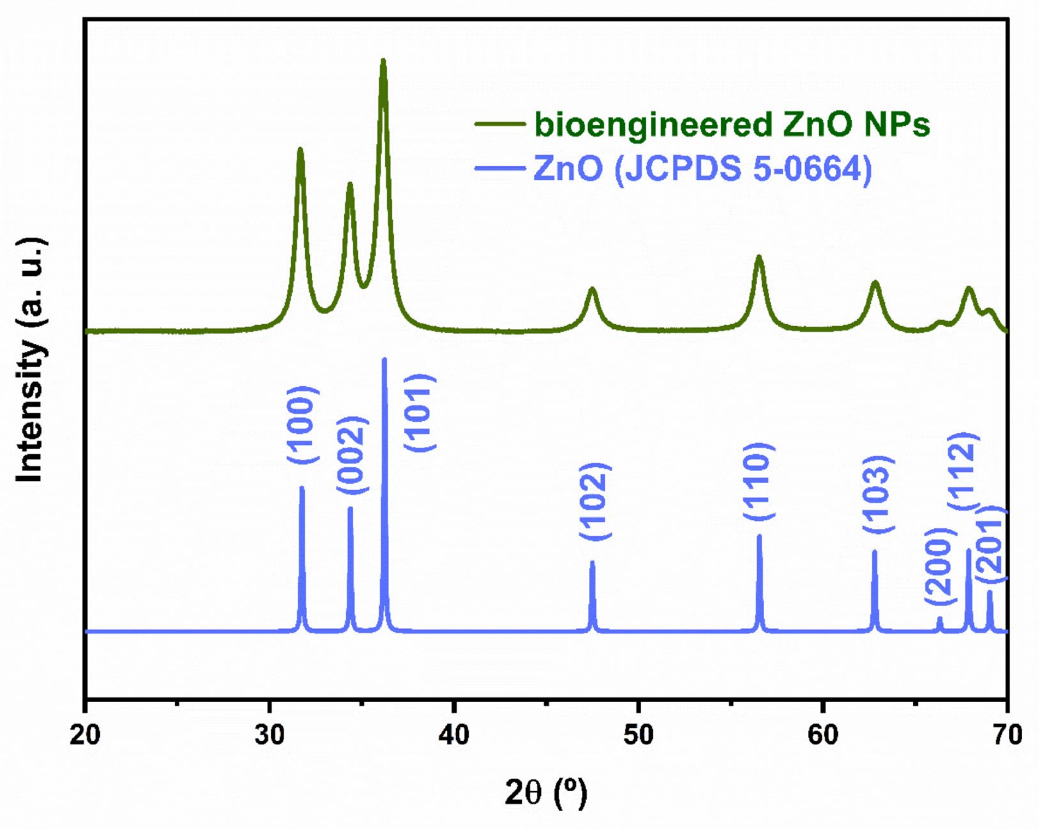

Fig. 1. - XRD patterns of the ZnO NPs synthesized using coffee leaves extract, revealing hexagonal wurtzite structure.

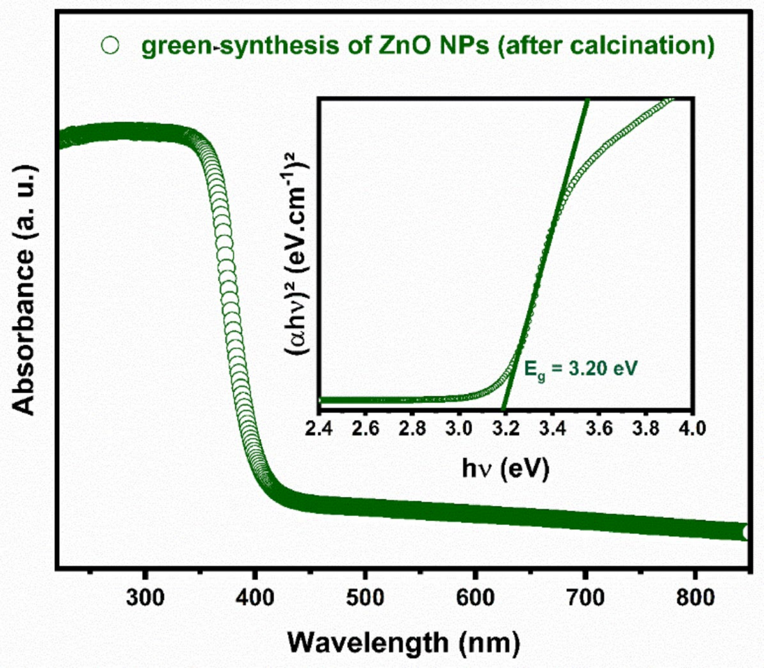

Fig. 2. Characterization of optical properties using UV-Vis absorption spectra of the bioengineered ZnO NPs. Inset shows the Tauc plot used for the optical band gap (E_g) determination.

conduction band (Zn 4s orbitals). Additionally, the band gap (E_g) of the ZnO NPs after sintering was estimated using the Tauc-Wood equation, considering ZnO as a direct transition semiconductor:

$$(\alpha h\nu)^2 = A\left(h\nu - E_g\right) \tag{2}$$

where α is the absorption coefficient, hν is the photon energy, and A is a constant.

The value of E_g was obtained from the linear extrapolation of the $(\alpha h\nu)^2$ versus hν plot (Tauc plot), resulting in an estimate of 3.20 eV. This estimated E_g value is lower than that of bulk ZnO (E_g = 3.37 eV), which can be attributed to quantum confinement effects, indicating that the ZnO particles are indeed in the nanometric range[42]. Although Tauc plot has a number of limitations, which can limit its applications for polycrystalline solids, including absorption tails, quantization effects, spectral overlap of different bands, excitons/many-body effects and optical transitions via localized charge carrier transfer[43] it continues to be widely used due to its simplicity. For example, previous studies of bioengineered ZnO NPs showed, using Tauc plots, that their optical bandgaps were in the 3.07–4.1 eV range[41,42].

Furthermore, the excitation of ZnO NPs under UV-A irradiation is expected to be productive, as the energy of UV-A light (λ_{max} = 368 nm and hν = 3.37 eV) exceeds the value of E_g and should lead to an efficient photocatalytic activity of the NPs. Therefore, as discussed below, potential applications of ZnO NPs for the photodegradation of a dye under UV-A irradiation were investigated.

SEM and EDS analysis

The surface morphology of the ZnO NPs produced using coffee leaves extract was explored using scanning electron microscopy (SEM) (Fig. 3A&B). The images were recorded at low and high magnification (at the scales of 1 µm and 200 nm, respectively). Topographical view shows that ZnO NPs are clustered together, forming the agglomerates. The agglomerates consist of approximately spherically-shaped ZnO NPs aggregated in clusters (Fig. 3A&B). Figure 3a shows a low magnification SEM image of the ZnO NPs, which exhibit a nearly spherical shape, a morphology frequently associated with green synthesis of ZnO NPs using plant extracts[44,45]. For a more detailed view and to estimate the average particle size, a high magnification SEM images were used (Fig. 3b).

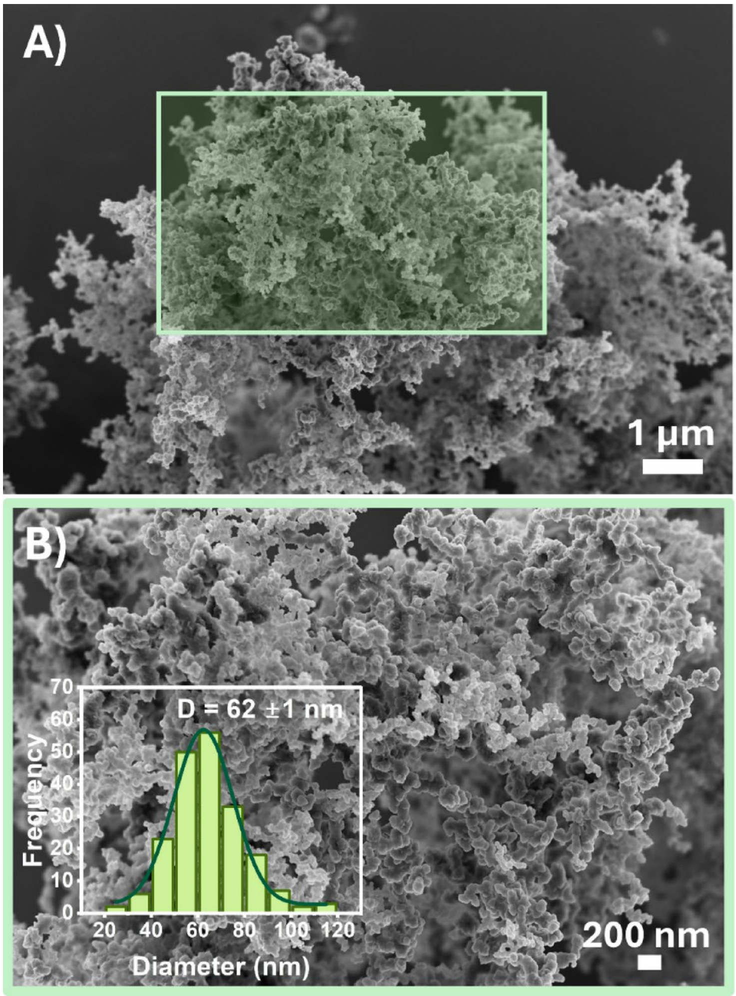

Fig. 3. FESEM images of the biosynthesized ZnO NPs: (**a**) at low magnification and (**b**) at high magnification.

The average size of the ZnO NPs was estimated by measuring the diameter of 200 NPs using ImageJ 1.54 g software. The ZnO NPs showed a broad size distribution ranging from 20 to 120 nm, with an average diameter of 62 ± 1 nm. Supplementary Table 2 summarizes ZnO NPs sizes synthesized using different plant extracts and conventional methods, including information on the synthesis method, NP sizes and their applications. One can see that the smaller particles in the microstructure of Fig. 3 tend to form more pronounced agglomerates compared to the larger particles. This phenomenon can be attributed to the greater specific surface area of the smaller particles, which promotes a higher density of interactions and, consequently, a greater tendency for agglomeration[46]. Comparison of the particle size computed from SEM measurements and the size of the ZnO crystallites determined by XRD, indicates that the particles observed by SEM are polycrystalline, resulting in a larger overall particle size as compared to the size of the individual crystallites[47]. The shape of the NPs plays a crucial role in their effectiveness against pathogens[48]. In particular, spherical NPs have been shown to be highly effective in antibacterial activity[49] due to their higher surface area-to-volume ratio, which enhances interaction with bacterial membranes, which this one of the applications investigated in this study.

In addition, energy dispersive X-ray spectroscopy (EDS) analysis was carried out (Supplementary Figure S1). The EDS analyses reveal the elementary composition of the synthesized ZnO NPs demonstrating the presence of three main chemical elements, one of which being gold, which has been deposited on the samples to enhance the electron conduction. The other two major signals correspond to Zn and O atoms. The EDS spectrum shows that the atomic and weight proportion for zinc and oxygen are 73.95% (92.06%) and 26.05% (7.94%) respectively. A tiny fraction of carbon, presumably from the extractives which remained imbedded in the samples after sintering, can also be observed (Supplementary Figure S1).

Dynamic light scattering (DLS) measurements

The hydrodynamic radio and particle size distribution of the biosynthesized ZnO-NPs were estimated using the DLS technique. DLS is a non-destructive light scattering analytical method which relies on the measurements of light intensity fluctuations over time due to particle Brownian motion[50].

This allows for determination of the diffusion coefficient (D), which is related to the hydrodynamic radius (R_h) of the particle via the Stokes–Einstein equation,

$$D = \frac{k_b T}{6\pi\,\eta\,R_h} \tag{3}$$

where k_b is the Boltzmann constant (1.380×10^{-23} kg m^2 s^{-2} K^{-1}), T is the absolute temperature, and η is the viscosity of the solution[50].

Thus, DLS results are influenced by solvent interactions and particle aggregation. The particle size distribution data from DLS measurements are given in Supplementary Figure S2. DLS results show that the average hydrodynamic radius (R_h) of NPs generated using coffee leaves extract is 58.85 ± 3.46 nm (Supplementary Figure S2), in line with the average particle size determined from SEM measurements. Comparison of these data with the XRD results reveal that hydrodynamic radii are significantly larger than the average crystallite sizes computed based on XRD data, thus supporting a notion that NPs contain several crystallite domains. The sample polydispersity index (PDI) was ~ 30.2%, confirming a relatively broad particle size distribution of the sample suspensions. In addition, the NP suspension also revealed relatively stable the hydrodynamic radii time-dependent distribution and, consistently, small time-dependent fluctuations (Fig. S2B).

DLS studies can provide more quantitative estimates of the biosynthesized ZnO NP aggregation. Here, we combined information provided by DLS about hydrodynamic radio of the bioengineered ZnO NP aggregates in solution with those provided by SEM about an average size of the individual NPs to figure out degree of NP aggregation.

From the SEM studies we know that an average diameter of the individual biosynthesized NP is 62 ± 1 nm (or radius of 31 ± 0.5 nm). This means that assuming spherical shape of the NP, its average individual volume is approximately 125 × 103 nm[3]. The DLS average hydrodynamic radius in solution is 58.85 ± 3.46mn. Assuming an average spherical size of the NP aggregates in solution and discarding a contribution from the solvent layer, an average volume of the NP aggregates is 853 × 10^{3}nm[3]. If we now presume that the later sphere is assembled by tightly packed incompressible spherical individual NPs, an average number of NPs per sphere is approximately 4. This means that an aggregate in solution is composed on average of four individual NPs with a mean radius of 31 nm each. It is important to stress that this is an estimate that is only valid within the scope of the above-mentioned assumptions. In real-life situations the aggregates can contain quite a significantly higher or lower number of individual NPs, depending on their actual size (which varies from 20 to 120 nm in diameter). Thus, for example, it could be a single big individual ZnO NP with a diameter of 120 nm or several dozens of small individual NPs with an average diameter of 20 nm grouped together, with a mean of size distribution at 4 average size ZnO NPs per aggregate.

FTIR ATR analysis

The contribution of functional groups from the phytochemicals present in coffee extract to the synthesis of ZnO NPs was identified through FTIR analysis, as shown in Fig. 4. The broad band with a peak centered around 3388 cm^{-1} in the FTIR spectrum can be attributed to the strong stretching vibrations of the hydroxyl group (-OH) present in phenolic compounds, flavonoids, and triterpenoids from the coffee extract[51]. In the FTIR spectrum of the extract, bands with peaks at 1315 cm^{-1} and 617 cm^{-1} indicate the presence of C–N stretching (aromatic amines) and alkyl halides[52]. Additional peaks at 1643 cm^{-1}, 1386 cm^{-1}, and 1037 cm^{-1} correspond to N–H bending of amines, C–H stretching of alkanes, and C–N stretching of aliphatic amines, respectively[53]. Similar bands were also observed in the synthesis of ZnO NPs, indicating the presence of the extract before the

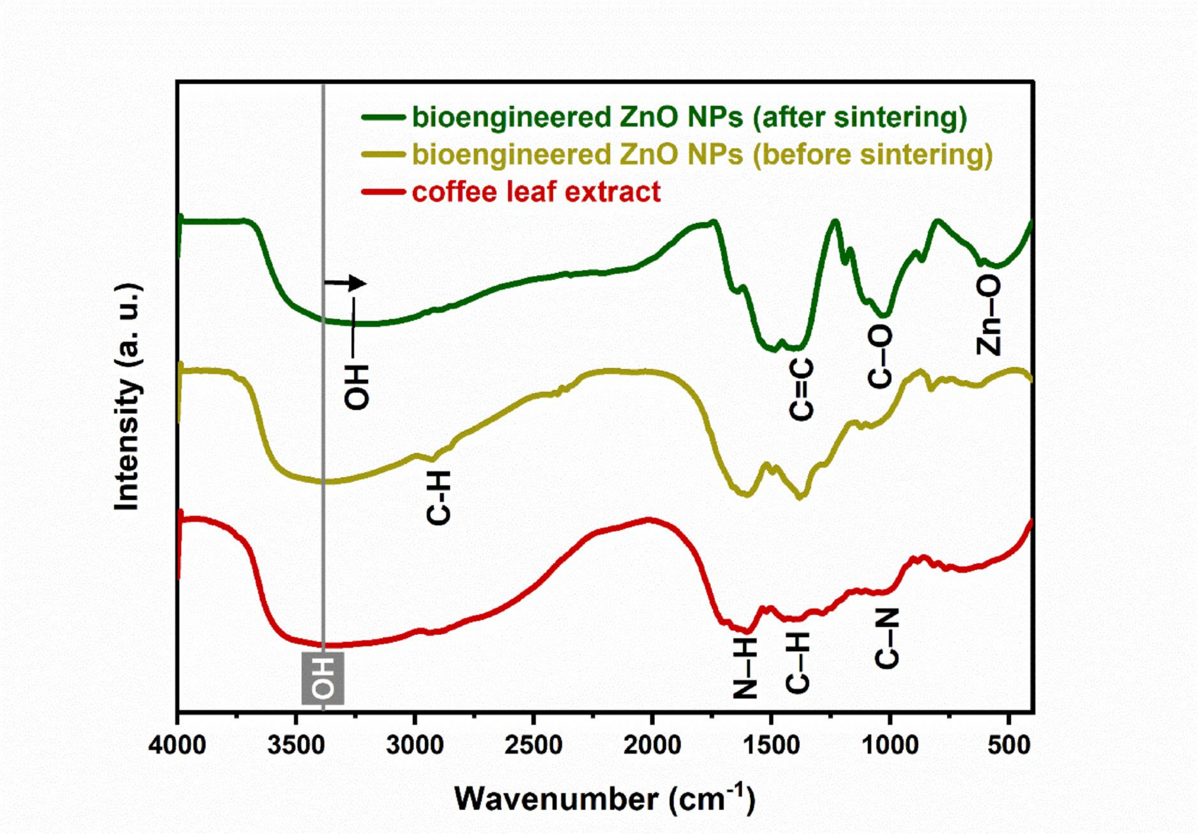

Fig. 4. FTIR spectra of coffee leaf extract and the bioengineered ZnO NPs (before and after sintering).

sintering step. However, the absence of bands related to Zn–O stretching in the 400–600 cm^{-1} region for the non-calcined sample suggests that sintering is necessary for the effective formation of ZnO NPs.

More significant changes were observed after sintering. The O–H band of the extract, associated with phenolic phytochemical compounds, shifted from 3388 to 3274 cm^{-1}, a statistically significant shift, indicating the involvement of these groups in the formation of ZnO NPs. For the calcined ZnO sample, the bands associated with the C = O stretching of the amide group (1652 cm^{-1}) shifted to 1607 cm^{-1}. The presence of a band corresponding to a primary amide suggests that the extract may bind to ZnO through carboxylate ions or free amine groups[54]. Further, the amide functional group may act as a stabilizing agent, reducing NP aggregation during growth. Additionally, bands in the range of 400 to 600 cm^{-1}, with a peak around 570 cm^{-1}, can be attributed to the stretching vibrations of Zn–O bonds, confirming the successful formation of ZnO NPs after sintering[55]. Therefore, sintering at 400 ºC provides sufficient energy to induce the nucleation and growth of ZnO NPs in the hexagonal wurtzite structure.

Thermogravimetric analysis (TGA)

The thermal behavior of the NPs up to 1000 °C is shown in Supplementary Figure S3. A relatively steep transition at ~ 80 °C, which corresponds to approximately 2% of mass loss, gives rise to comparatively featureless slow descent until approximately 850 °C, where a second transition occur. The first loss is related to the evaporation of water molecules physically bound to the ZnO NPs, while the second weight loss can be attributed to the removal of the residual organic material, CO_2 desorption from the materials surface and the reorganization of ZnO NPs[56,57]. This behavior is consistent with the results of FT-IR analysis (Fig. 5A) which demonstrates both a presence of water as well as reminiscent organic compounds originating from the coffee leaves extractives. A total weight loss of ZnO NPs is approximately 4%, demonstrating that a number of organic molecules present in the NPs is small. Thus, TGA reveals that the synthesized ZnO NPs are thermally stable and their heating up to 1000 °C does not lead to any significant weight loss. When compared with other bioengineered ZnO NPs, the observed weight loss is indeed very small. For example, TGA profile of ZnO NPs obtained via *Moringa oleifera* green synthesis exhibited a continuous weight loss of almost 60%, with 3 quasi sharp changes occurring at 139, 223, and 392° C[56]. In another study, ZnO NPs synthesized using *Eucalyptus globulus* Labill. leaf extract lost almost 66% of the initial mass upon heating to 700°C[58].

On the other hand, comparison of the heating stability of the bioengineered ZnO NPs obtained in present study with CeO_2 NPs[59], TiO_2 NPs[60,61] and $CoFe_2O_4$ NPs[62] reveal equal or superior stability of the green ZnO NPs obtained in current study as judges by TGA analysis.

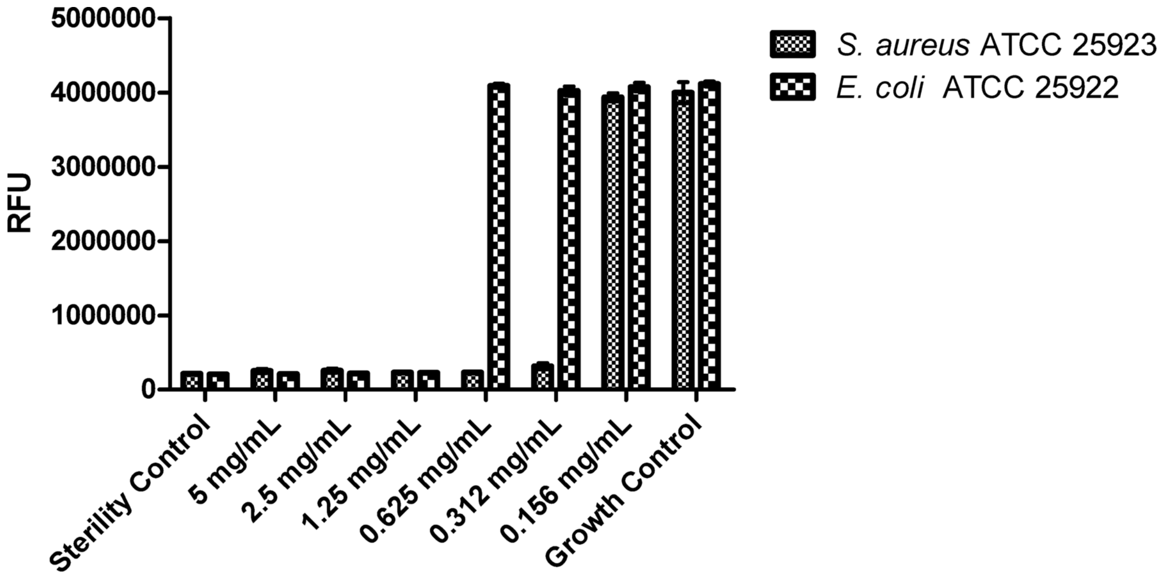

Fig. 5. Bacterial cell viability in the presence of the ZnO NPs measured by the resazurin assay. RFU: Relative Fluorescence Units.

Electron spin resonance (ESR) analysis of the obtained NPs

ESR has proved to be a powerful technique to probe zinc and oxygen vacancies, dopant effects, and to understand the spin system in ZnO[63–66]. To assess the quality of our ZnO particles in terms of defects and vacancies, we conducted ESR measurements at room temperature. ESR signals can be attributed to the Zn vacancies[63,64], spin canting effects[65,66], etc. The ESR spectrum from the ZnO NPs synthesized using coffee leaves extract are given in Supplementary Figure S4. The synthesized ZnO particles demonstrate a g value of 2.0437. This g-value indicates that the ESR signals can be attributed to the Zn vacancies[63,64].

Applications

Antibacterial activity of the synthesized NPs

ZnO NPs have unique physicochemical characteristics that can affect biological and toxicological responses of microorganisms. ZnO NPs have been extensively used in various biomedical fields including antibiotic therapy, medical devices, theranostics, tissue engineering, and health care because of their antimicrobial characteristics[67]. Here, the bactericidal activities of the green ZnO NPs were tested against two main clinical pathogens: Gram-negative bacteria *E. coli* and Gram-positive bacteria *S. aureus*.

The synthesized ZnO NPs interfered with both *E. coli* and *S. aureus* growth. The minimum inhibitory concentration (MIC) for *S. aureus* ATCC 25,923 was 0.312 mg/mL (Fig. 5), since this concentration was sufficient to lower the viability of the microbial cells to the sterility control level, as detected by the resazurin assay. On the other hand, considerably higher concentrations of ZnO NPs were required to inhibit bacterial growth of *E. coli* ATCC 25,922 bacterial strain. Here, MIC was 1.25 mg/mL, as depicted in Fig. 5. One can observe that in the presence of the bioengineered ZnO NPs at concentrations lower than 1.25 mg/mL, *E. coli* cells were able to metabolize the resazurin molecule to the fluorescent resorufin at the same rate as the growth control, and when concentration equals to 1.25 mg/mL or higher, the fluorescence level was similar to the sterility control, meaning that no metabolically active bacterial cells were present.

The antimicrobial activity of ZnO NPs can be explain by the release of zinc ions, generation of reaction oxygen species (ROS) and induction of changes in the permeability of the bacterial cell membrane[68,69]. The release of Zn^{2+} from the NPs has the antibacterial activity since the released Zn^{2+} can bind to proteins, carbohydrates and DNA, disrupt enzymatic activities, and inhibit active transport and amino acid metabolism in bacterial cells, which has negative effect on cell viability[68]. Furthermore, ROS generated by the NPs have the capability to disrupt microbial metabolism by affecting DNA/RNA, proteins, and lipids, which results in inhibition of bacterial growth and cell death[70].

Additional potential mechanisms involve the impairment of the bacterial envelope, inhibition of the respiratory chain, and fragmentation of nucleic acids. Indeed, the accumulation of ZnO NPs in the cell membrane leads to the dissipation of the proton motive force and causes changes in the permeability of the plasma membrane, which results in the progressive release of lipopolysaccharides, proteins, and intracellular components from the bacterial cell, reducing cell viability[70].

While ROS-mediated mechanisms are commonly associated with ZnO NP antimicrobial activity, recent studies suggest that alternative pathways, such as metabolic perturbations, may also play a significant role, particularly in methicillin-resistant *S. aureus* (MRSA) strains[71]. For example, ROS-independent antibacterial activities have recently been reported for PtCuTe nanosheets[72] and gold NPs[73]. Furthermore, it was shown that ZnO NPs caused significant up-regulation of pyrimidine biosynthesis and carbohydrate degradation pathways. Simultaneously, amino acid synthesis in the *S. aureus* strain was significantly down-regulated[71]. This indicates a complex mechanism of antimicrobial resistance, involving multiple metabolic pathways. Whether similar mechanism applies to *E. coli* and other bacterial pathogens still remain to be seen.

Numerous studies have utilized agar diffusion techniques to investigate antimicrobial properties of NPs[74]. However, in line with the observations of Rutherford et al.[75] our investigations did not reveal significant inhibition of bacterial growth when the agar diffusion methodology was used (data not shown). This might be attributed to the absence of interacting kinetics between NPs and bacteria. It is known that traditional techniques such as agar diffusion, commonly utilized in antimicrobial assays, may encounter limitations including lack of reproducibility and only produce qualitative results[76]. A diverse array of more advanced antimicrobial assays including resazurin assay, bioautography, co-culture, flow cytofluorometric and bioluminescent methods, to name a few, can be viable alternatives to agar diffusion assays. To ascertain the effective inhibitory concentration of NPs, the resazurin broth dilution method, applied in present study, is recommended[77].

Other authors have previously noted the higher sensitivity of *S. aureus* to ZnO NPs compared to *E. coli*[78,79]. This phenomenon can be attributed to differences in their cell membrane polarities. *S. aureus* membrane is less negatively charged than that of *E. coli*, potentially enhancing the penetration of the negatively charged free radicals. Other studies found no differences in MIC of NPs between Gram-positive and Gram-negative species or even higher sensitivity of the latter bacteria[80,81]. This can be related to the size of the NPs and other experimental conditions[82]. Indeed, it was shown that smaller ZnO NPs has stronger antimicrobial effects[82].

The MICs of the green-synthesized ZnO NPs against *E. coli* and *S. aureus* are similar to those reported in studies using chemically synthesized ZnO NPs. Emami-Karvani and Chehrazi (2011) found that 1 mg/mL was sufficient to inhibit the growth of *E. coli*, while 0.5 mg/mL effectively inhibited *S. aureus*[78]. Likewise, Mirhosseini and Firouzabadi (2013) reported that 10 mM of ZnO NPs, equivalent to 0.81 mg/mL, could inhibit the growth of both *E. coli* and *S. aureus*[83]. More recently, Balayevska et al. (2022) found that similar concentrations of ZnO NPs were required to inhibit these bacteria: 0.5 mg/mL for *E. coli* and 0.25 mg/mL for *S. aureus*[84].

Therefore, one can conclude that the bioengineered ZnO NPs are as effective as their chemically synthesized counterparts, while offering an advantage of environmental sustainability.

Photodegradation effects of the green ZnO NPs

ZnO NPs have several properties important for photodegradation, including high efficacy in removing chemical compounds, cost-effectiveness, harnessing of available light for their antibacterial activity and elevated efficiency of organic dyes and other pollutants photocatalytic degradation[85]. The temporal evolution of absorbance spectra during a photocatalytic experiment using ZnO NPs for the degradation of a 5 mg/L methylene blue (MB) solution is shown Fig. 6a. The characteristic MB peak in the UV-Vis region at 664 nm was used to monitor the relative concentration of MB in the solution[86]. This absorption peak is attributed to the $n \rightarrow \pi^*$ electronic transition[87]. In the presence of ZnO NPs, the absorbance and, consequently, the concentration of MB decrease over time. This reduction in absorption intensity at 664 nm can be attributed to the ROS-mediated oxidation of chromophores and destruction of the chromophore groups responsible for the color[88].

Figure 6b illustrates the variation in the relative concentration of MB over time. It is evident that adsorption-desorption equilibrium has been reached, with the removal of MB by adsorption onto ZnO NPs being around 6%. On the contrary, the removal rate, combining the synergistic effects of adsorption and photocatalysis by ZnO NPs, was 72%. This demonstrates the predominant role of photocatalysis over adsorption in the degradation of the dye.

Exposure of the MB solution to UV-A irradiation, in the absence of ZnO NPs, resulted in insignificant degradation of the dye (Fig. 6c), with only 2.1% degradation after 120 min. In contrast, the presence of ZnO NPs resulted in a significantly higher degradation efficiency of 70.2%, underscoring the potential of the ZnO NPs for dye degradation. The degradation of MB can be described by the pseudo-first-order kinetic model:

$$-\ln\left(\frac{C_t}{C_0}\right) = kt \tag{4}$$

where C_0 and C_t represent the concentration of MB after reaching adsorption-desorption equilibrium and the concentration at a given time t, respectively. The slope of the line obtained from the plot of $-\ln(C/C_0)$ versus time allows for the determination of the kinetic constant (k). The value of k for the photocatalysis experiment is approximately 100 times greater than for the photolysis experiment, which reinforces the effectiveness of ZnO NPs in the degradation of MB (Fig. 6d). Additionally, the high linear correlation coefficients (R^2) obtained suggest that the data fit well with the pseudo-first-order kinetic model. Kinetic constant determined in present study is similar to the previously determined kinetic constants for ZnO NPs degradation of MB[89]. Furthermore, kinetic constants of 0.018 min^{-1} for methyl orange (MO) and 0.014 min^{-1} for MB were observed using cerium oxide NPs synthesized using *Portulaca oleracea* extract[90]. Moreover, photodegradation of MB by cobalt oxide NPs followed first-order kinetics with rate constant of 0.0065 min^{-1} [91]. Photocatalytic degradation of environmental pollutants using copper oxide NPs reveals first-order kinetics rate constants for p-nitrophenol and MB pollutants, exhibiting maximum apparent rate constants in the range of 0.1003 min^{-1} up to 0.5100 min^{-1} depending on the concentration of the nanocatalyst and type of pollutant[92–94].

The plant extract mediated green synthesis of metal oxide NPs is attracting growing interest due to its cost-efficiency and environmental friendliness. ZnO NPs have elevated photocatalytic activity and are actively studied for the removal of water pollutants via photocatalytic degradation, reduction reaction, and adsorption mechanism[95].

Other bioengineered metal particles, such as gold nanosperes[96] and silver nanoflowers[97] have also been successfully used for organic dye degradation in recent years.

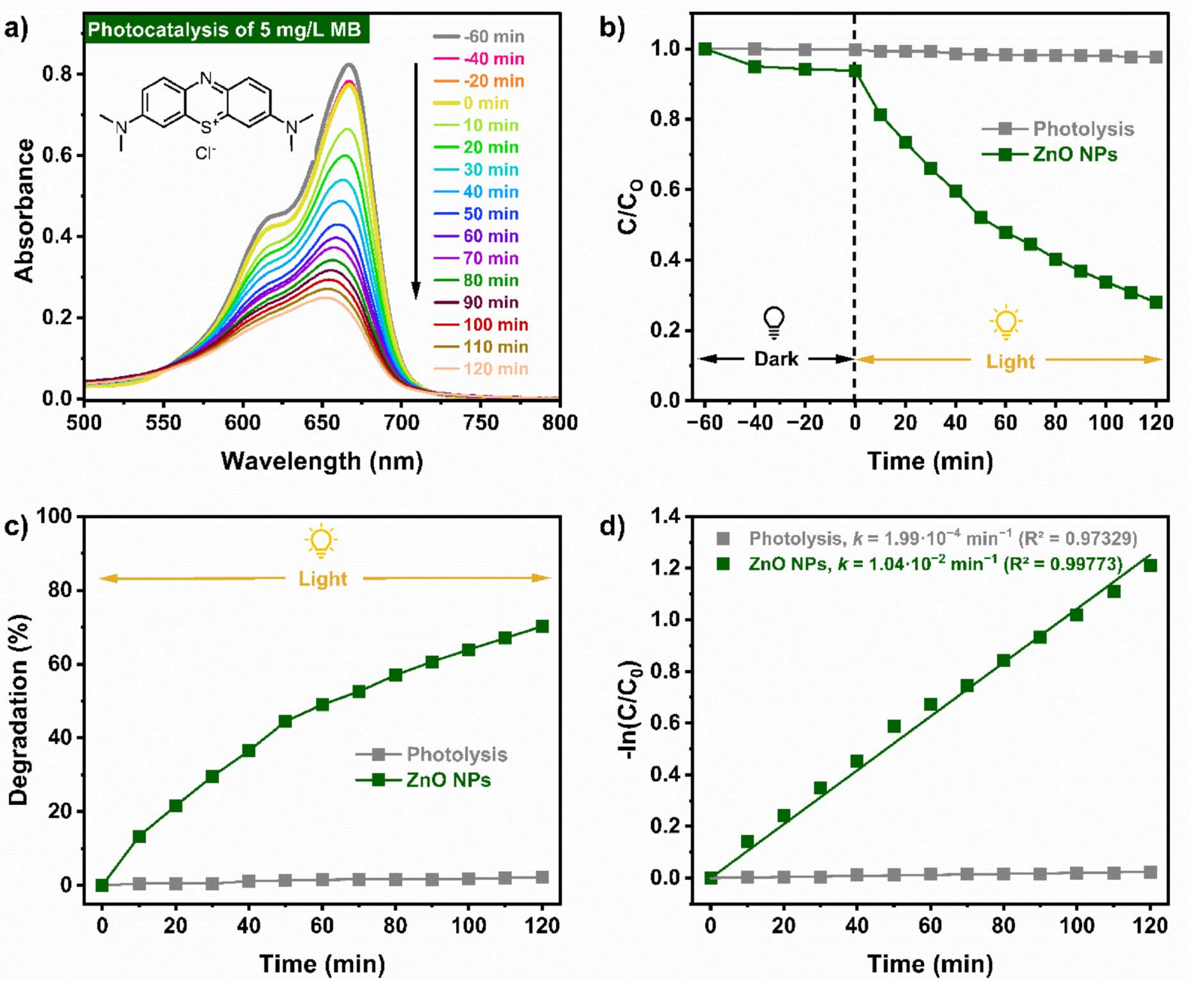

Fig. 6. (**a**) Variation of MB absorbance as a function of time; (**b**) Plot of C/C_0 versus time in the presence and the absence of the ZnO NPs; (**c**) Degradation efficiency in the presence and in the absence of the nanocatalyst; (**d**) Plot of $-\ln(Ct/C_0)$ versus time for the degradation of MB dye with and without ZnO NPs catalyst under UV-A irradiation. Experimental conditions: C_0 = 5 mg/L of MB, 0.25 g/L of photocatalyst, and T = 25 °C.

Use of green ZnO NPs for BioReRAM assembly

ZnO has found extensive use in resistive switching memory (ReRAM) applications. ReRAM is a new class of memory, based on switching of resistive states and is emerging very fast, since it offers extreme low power operation and light weight. Here, we attempted to further expand into the ‘green computing’ with the possibilities of a biodegradable green bioReRAMs, prepared using renewable components and sustainable methods. In present work, bioReRAM was successfully manufactured by using the drop casting method, followed by drying it at room temperature, e.g. the process did not require any heat or electricity. The best results were obtained by adding 0.025 g of ZnO to 0.1 g of chitosan.

Chitosan is abundant and easily prepared from chitin, natural polymer found in insect and crustacean cells. Chitosan is a cationic polymer, which allows decoration and functionalization, for example, with ZnO NPs[98]. Moreover, chitosan has an excellent film-forming ability combined with good mechanical strength and flexibility and can be used for disposable device applications and flexible wearable electronics[99]. All these properties are attractive for the development of highly performing bioReRAMs.

ZnO, like many other metal oxides, has the ability to improve BioReRAM electrical conductivity. However, the device switchable (reversible) resistance states, rather than just electrical conductivity, are what enable resistive switching in ReRAMs. ZnO might contain oxygen and zinc vacancies, which are necessary to enable resistive switching in bioReRAMs[100].

Indeed, our ESR analysis (g-values of ESR signals) shows that Zn vacancies are present in our bioengineered ZnO NPs. Both oxygen and Zn vacancies have significant influences on the electrical properties. It is well established that the free-carrier concentration has a direct linear relation with the density of oxygen vacancies. Furthermore, excessive concentration might have an opposite effect, i.e., increasing the resistivity of ZnO[100].

Further, if oxygen vacancies increase sufficiently, they might become trapping centres, and trapped charge limited conductivity (TCLC) can kick in. In some of the ReRAMs, TCLC behaviour was well established[101]. As to the influence of Zn vacancies, as evident from our ESR characterization, Zn vacancies are supposed to give rise to p-type conductivity. However, it was established that Zn vacancies in combination with other defects, make the situation more complex. Thus, in the context of ReRAM and resistivity switching, the Zn and oxygen vacancies can act as traps and might lead to TCLC behaviour.

To understand the memory behaviour in the Ag/chitosan-ZnO/ITO-PET bioReRAM, the Ag electrode was connected to the word line (WL), and the ITO electrode was connected to the bit line (BL). A pulsing voltage was applied to the WL while the current at the BL was measured. The voltage pulse followed a staircase pattern, starting at 0 V and increasing in steps of 0.05 V. Each pulse had a pulse width of 50 ms and an interpulse time of 10 ms. The voltage was gradually increased until it reached a predetermined maximum value in both the positive and negative polarities and was swept back to zero to complete a full cycle. After each pulse, a constant readout voltage of 0.5 V was applied to measure the current response.

Figure 7A depicts the changes in current-voltage (I-V) during the first scan cycle (with +/- 5 V amplitude) of our bioReRAM. The graph indicates that with an increase voltage in the positive bias (Region 1), the current rises steadily from + 1.2 V (i) to around 2.5 microamperes. Throughout the downward sweep in the same bias (Region 2), there was a noticeable linear decrease in current with voltage along a distinct path, resulting in an I-V hysteresis. The linear behaviour persists briefly during the negative bias (Region 3) until a deviation occurs at −0.7 V (ii). Based on the observed data, it appears that the current initially decreases as the voltage increases, but then it later increases again along a different path. The current follows this new path during the downward sweep in the Region 4, eventually reaching zero at −1.7 V (iii). We plotted the same date on a semilogarithmic scale, as depicted in Fig. 7B. This graph clearly shows a decrease in current during the negative bias, suggesting that the device is resetting. However, there is no distinct sudden increase in current observed in the graph, which could indicate the set process. After conducting 10 consecutive scans, the current-voltage (I-V) behaviour showed consistent results (Fig. 7C). Furthermore, we carried out a similar experiment using circles with 10 V amplitude, and the results revealed similar hysteresis with no obvious voltage scan amplitude dependence. We also conducted the endurance study and obtained the best result when using ± 10 V pulse, with a pulse width of 100 microseconds, 0 s interpulse time, and the readout voltage of 2 V. Based on our findings, it is evident that the device's ON and OFF states remain constant. Furthermore, the device is reliable for more than 2000 write/erase cycles, as demonstrated in Fig. 7D. Moreover, the cumulative probability plots of both the HRS and LRS show that the two states are fairly stable (Fig. 7E). The ratio of R_{ON} (Resistance in the ON state) to R_{OFF} (Resistance in the OFF state) is determined to be 3.

Next, we looked into data retention behaviour of the device (Fig. 7F). The data we have collected (Fig. 7A) exhibit fluctuations in both ON and OFF state resistance over time. These fluctuations increased notably beyond the 100-second mark, leading to the RON/ROFF ratio approaching zero. Similar device limitation was recently reported by Deb et al. in Al/7HNO3C + ZnO/ITO[102]. Furthermore, large fluctuations were observed by Simanjuntak and collaborators[103] in the endurance data for the Cu/ZnO/ITO device. At the same time, earlier Patil and colleagues reported an Ag/ZnO/FTO ReRAM device with stable endurance for over 10^3 write/erase cycles and retention for over 10^3 s[104]. Based on these reports, we are optimistic that optimization of the experimental parameters can lead to the device improvement. For example, Xu and collaborators stalked ZrO_2 and ZnO layers to improve the memory behaviour[105]. The order of the layer stalk has been shown to strongly affect the memory behaviour. A similar effect has also been shown prior by Ismail and colleagues[106] for the ReRAM consisting of CeO_2 and ZnO layers. Similar ideas can be employed to improve our device in the future.

It is important to notice that chitosan-ZnO composite utilized in this work has different characteristics from the commonly used plain ZnO. Plain ZnO-based ReRAMs are frequently called oxyReRAMs because, like all metal oxide-based ReRAMs, they function by using oxygen vacancies and thus deteriorate more rapidly. ZnO is used in this work to improve chitosan-based active layer conductivity and to create resistive switching behaviour. However, the bioengineered ReRAM switching mechanism is independent of oxygen vacancies. The drop cast process was used the bioReRAM fabrication since it eliminates a need for heating or electricity. This concept was developed to guarantee that our green synthesized ZnO NP-based device could be produced at very low costs. Moreover, compared to active layers deposited using other techniques such as spin coating, the drop cast approach is held accountable for producing active layers with a higher thickness. In the follow up studies, one can further improve the ON/OFF ratio by optimizing a thickness of the active layer.

By understanding the underlying principles governing current behaviour in different regions shown in Fig. 8A, one can tailor their optimization strategies to enhance device performance. In Fig. 8B, the data for the ON state (Region 2) is shown to have a linear relationship (Ohmic: $I \propto V$), while in the Region 1, a power function ($I \propto V^2$) best fit the data. This mechanism is similar to the one observed for the Al-doped ZnO incorporated PMMA system with Ti and ITO top and bottom electrodes, respectively, where hopping conduction was proposed[107].

Conclusions

Here we successfully synthesized green ZnO NPs using fresh coffee leaves extract. The NPs were thoroughly characterized using a number of analytical techniques, including XRD, DLS, UV-Vis, FT-IR, SEM, EDS, TGA and ESR. Their antimicrobial applications and photodegradation effects have been evaluated. Furthermore, for the first time, the resistive switching behavior of chitosan polysaccharide doped with the synthesized green ZnO NPs was demonstrated. This opens up the opportunities for biological Resistive Random-Access Memory (bioReRAM) production. Possible future research directions include bioReRAM stability optimization, use of alternative biopolymers and other metal oxide NPs for bioReRAM assembly, as well as exploring other plant-based sources for green synthesis of the metal oxide NPs.

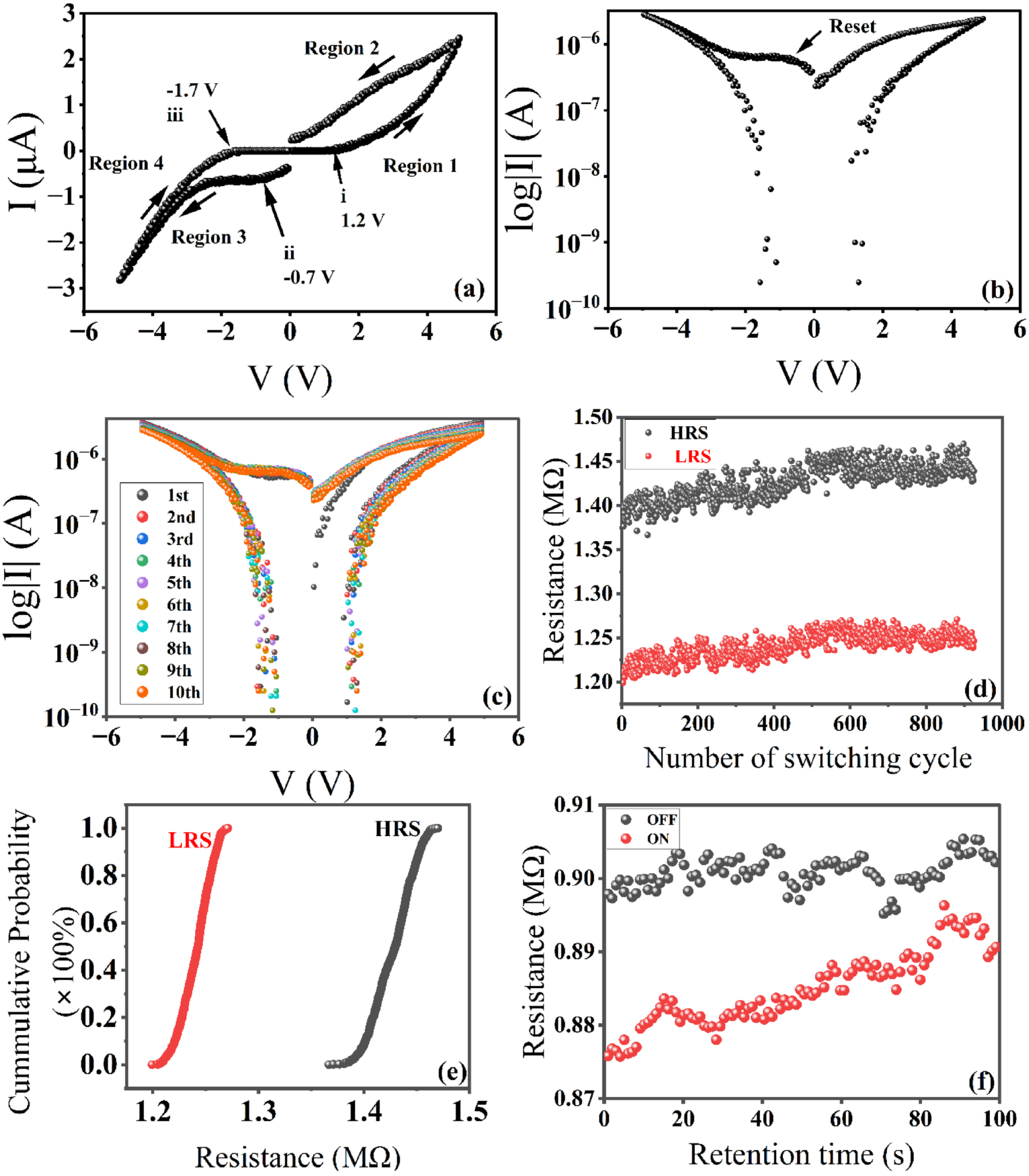

Fig. 7. Memory characterization results for the Ag/chitosan-ZnO/ITO-PET device. The I-V graph during the first voltage scan cycle plotted on the linear scale (**a**), and on semilog scale (**b**); whereas (**c**) shows the variation across the first ten cycles on the semilog scale. (**d**) Resistance of the RHS and LRS at different switching cycles; (**e**) Cumulative probability plots for the resistances of the device at HRS and LRS, respectively, as based on (**d**). (**f**) The data retention graph for the Ag/chitosan-ZnO/ITO-PET device.

Materials and methods

Plant extract Preparation and NP synthesis

Fresh leaves from coffee tree (*Coffea arábica L.*) were collected at a local farm (Araraquara, SP, Brazil). The leaves were washed with distilled water to remove impurities. Next, the leaves were dried at 40 °C until humidity dropped below 10%. Finally, the dried leaves were milled with a knife mill to approximately 20-mesh and stored in plastic bags at room temperature until their usage. The phytochemical water extractions were carried out using 20 g of dried and milled leaves, mixed with 200 mL of Milli Q water. The mixture was taken to autoclave

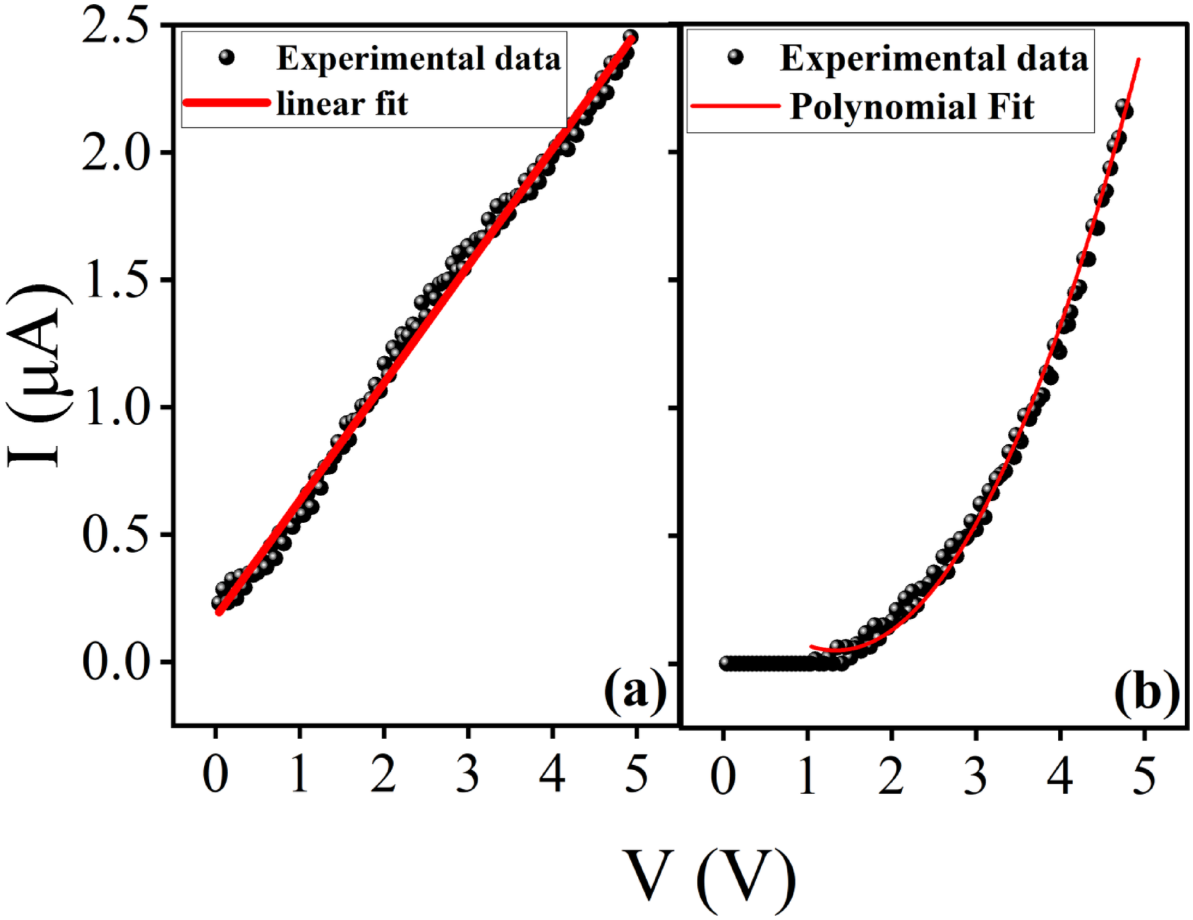

Fig. 8. The Ag/chitosan-ZnO/ITO-PET device's I-V data simulation of region 2 using linear function (**a**) and region 1 using power function (**b**).

and heated to 121 °C for 30 min. The solid residues were discarded, and the extractives were recovered by filtration. The final volumes for the coffee leaf water-soluble extracts were adjusted to 150 mL.

Zinc nitrate hexahydrate (Sigma-Aldrich) was used as a ZnO NP precursor, in the ratio 6:100 (m/v). After the salt dissolution, pH of the solution was measured and adjusted to 6.5 using sodium hydroxide at 6.5 M concentration. The mixture was taken again to autoclave and kept at 121 °C for 1 h. Next, it cooled down to room temperature and centrifuged at 13,000 rpm for 15 min at 25 ºC. The supernatant was discarded and the solid residue collected and extensively washed with water. The washing was performed twice to clean the particulate. The recovered solid fraction was placed in an oven and kept at 105 ºC during 24 h to lower the moisture. Finally, the green synthesized ZnO NPs were obtained via sintering in a muffle at 400 °C for 4 h. The protocol of green ZnO NP synthesis has been repeated multiple times, leading to consistent and reproducible results.

Characterization of ZnO NPs

X-ray diffraction analyses

XRD measurements were performed using a Miniflex 600 X-ray diffractometer (Rigaku, Japan) operating at 40 kV and 15 mA, employing Cu Kα radiation ($\lambda = 1.5406$ Å). The experiments were conducted at an ambient temperature. Detection covered the 2θ range from 5 to 70°, with a step interval of 0.02° and an exposure time of 15 s per step. The individual diffraction peaks were extracted by a curve-fitting process from the experimental diffraction scans. Peak fitting program (PeakFit; www.systat.com) was used to adjust Gaussian functions for each peak and the particle average crystallite sizes were estimated by using the Scherrer Eq. 1[08].

UV-Vis spectrophotometric measurements

The optical properties of the ZnO NPs were characterized using UV-Vis spectrophotometer in a diffuse reflectance mode within the wavelength range of 220 to 850 nm (Shimadzu UV-2600i, Japan).

From the spectrum acquired, the NP band gap was calculated using the Tauc plot for the direct band gap, as following:

$$(\alpha\, h\nu\,)^{1/n}\ =\ A * (h\nu\ - Eg\,)$$

where α is an absorption coefficient, A is constant, hν is the photon energy and E_g is bulk band gap, for direct allowed transitions: $n = 1/2$, for direct forbidden transitions: $n = 3/2$, for indirect allowed transitions: $n = 2$ and for indirect forbidden transitions: $n = 3$[109]. Typically, the allowed transitions dominate the basic absorption processes, giving either $n = 1/2$ or $n = 2$, for, respectively, direct and indirect transitions. The band gap was obtained by the extrapolation of a linear regression to X-axis of the plot with $n = 1/2$ since ZnO is well known to have a direct allowed transition.

SEM and EDS analyses

The morphological characteristics of prepared ZnO NPs were recorded using scanning electron microscopy (SEM) technique. The morphologies of the powders were analyzed using on field-emission scanning electron microscope (FESEM SUPRA™35, Carl Zeiss, Germany) operating of 5 kV. The samples were prepared as 1 mg/mL solution in ethanol and dried on the sample holder.

The elements present in the synthesized NPs were determined by energy-dispersive X-ray spectroscopy coupled to a scanning electron microscopy (SEM-EDS) (Zeiss, LEO 440, Germany). The ZnO NP powder was applied over a carbon tape and coated with a thin layer of Au using a sputter coater.

DLS measurements

DLS technique was employed for the determination of hydrodynamic radii and particle size distribution of synthesized ZnO NPs. NPs were diluted in deionized water was analyzed using a SpectroSize 300 instrument (XtalConcepts, Germany) at 660 nm wavelength. 15 µL of the sample were loaded into a closed quartz high precision cell (Hellma Analytics, Germany; light path: 1.5 × 1.5 mm). Twenty measurements each for 20 s duration were recorded, and the autocorrelation functions were analyzed by the CONTIN algorithm. During these measurements a correlation function is computed, which depicts the rate of fluctuations in the intensity of scattered light due to the Brownian motion of NPs. From the correlation function the particles size distribution is obtained. For the analysis ZnO NPs were diluted as 1% w/w water dispersion.

FT-IR analysis with ATR

FTIR spectrometer (Nicolet 6700) was used to classify functional groups in the synthesized ZnO NPs. Analyses were performed in the range of 4000–400 cm$^{[-1}$ at a room temperature. The pellets contained 250 mg of KBr (Sigma-Aldrich) and 12 mg of ZnO NPs and were prepared by applying a pressure of 50 kN/m^2 for 5 min.

TGA of the bioengineered ZnO NPs

TGA measurements were carried out using a Mettler Toledo thermogravimetric analyzer for the investigation of thermal stability. For the above purpose, 10 mg of the tested sample was decomposed by heating it from room temperature to 1000 °C at 10 °C/min heating rate under synthetic air flow.

ESR characterization of NPs

ESR spectra of ZnO provide valuable information about nanomaterials. ESR measurements were carried out at 9.38 GHz, room temperature, using a Bruker spectrometer, with a modulation field at 100 Hz.

Applications of the plant-derived ZnO NPs

Antibacterial activity of the NPs

The Minimum Inhibitory Concentration (MIC) of ZnO NPs was determined for both, the Gram-positive coccus *Staphylococcus aureus* ATCC 25,923 and the Gram-negative bacillus *Escherichia coli* ATCC 25,922 using the CLSI microdilution methodology with adaptations.

In brief, the NPs were prepared as 10-fold concentrated stocks in sterile water, and the bacterial inoculum contained 5×10^6 CFU/mL. One hundred and sixty microliters of Mueller-Hinton broth were dispensed into the wells of a 96-well microplate, and 20 µL of the ZnO NP suspension were added to the respective well. Subsequently, 20 µL of the inoculum were introduced into the wells, resulting in a final concentration of 5×10^5 CFU/mL. Sterility control (culture medium only) and growth control (culture medium + inoculum) samples were also included. Each NP concentration was tested in triplicate, ranging from 5 to 0.156 mg/mL through a 2-fold serial dilution. The microplates were then incubated for 24 h at 37 °C.

After incubation, we employed the resazurin fluorescence assay to determine the MIC, as the turbidity of the medium caused by the presence of NPs made it challenging to distinguish from the turbidity produced by bacterial growth. The resazurin assay is based on the ability of viable microorganisms to reduce the non-fluorescent resazurin molecule to the fluorescent resorufin. The level of fluorescence generated is proportional to the number of viable cells[109]. Briefly, wells in a 96-well black microplate were filled with 100 µL of the content from the microdilution experiment, plus 20 µL of a 0.15 mg/mL resazurin solution. The plate was incubated for 4 h at 37 °C, and fluorescence was measured in a Biotek Synergy H1 microplate reader (Agilent, United States) using excitation at 550 nm and emission at 590 nm[110]. The MIC was defined as the smallest concentration producing fluorescence at the same level as the sterility control.

Evaluation of ZnO NPs photocatalytic activity

The photocatalytic activity of the calcined sample, obtained through the green synthesis of ZnO NPs using coffee extract, was evaluated using MB as a model pollutant. In a typical photocatalysis experiment, 25 mg of the photocatalyst was dispersed in 100 mL of aqueous MB solution with a concentration of 5 mg/L. To achieve adsorption-desorption equilibrium, the mixture was stirred in the dark for 60 min. After this dark period, the mixture containing MB and the photocatalyst was irradiated with UV-A light for 120 min, using six UV-A F15T8/BL Blacklight lamps (Sylvania, Germany), each with a power of 15 W and a maximum wavelength of

368 nm. During the experiment, 1.5 mL aliquots were taken every 10 min. The supernatant was collected by centrifugation at 15,000 rpm for 10 min. The degradation of the pollutant was monitored by measuring the decrease in the maximum absorbance of MB in the supernatant, with a peak centered at $\lambda = 664$ nm, using a UV-Vis spectrophotometer (Kasuaki IL-593). As a control, a photolysis experiment was conducted under the same conditions as the photocatalysis experiment but without the photocatalyst. The degradation rate was calculated using the following equation:

$$\%\ Degradation = \left(\frac{C_0 -\ C_t}{C_o}\right)*100$$

where C_0 represents the initial concentration of the MB dye (after equilibrium) and C_t is the concertation after UV-A irradiation at a given time t.

Use of green ZnO NPs for BioReRAM assembly

ZnO NPs were synthesized using a green synthesis method and combined with chitosan, a biopolymer, to create a flexible bioReRAM device. A solution of chitosan was prepared by dissolving 0.1 g of chitosan in 10 ml of ultra-purified water. This solution was then mixed with 0.025 g of the synthesized ZnO NPs. The composite solution was thoroughly mixed for 1 h to ensure even distribution of ZnO NPs within the chitosan matrix. The solution was carefully applied onto a clean indium doped tin oxide (ITO) layer that had been previously deposited on a poly (ethylene terephthalate) (PET) substrate. The solution was left to dry at room temperature for 48 h. The shadow mask method was used to deposit top silver (Ag) contacts using Ag paste. The device was allowed to dry for more than 24 h prior to characterization. The configuration of the final device is Ag/chitosan-ZnO/ITO-PET, where Ag is top electrode, chitosan-ZnO is the switching active layer and ITO is bottom electrode on the PET substrate. The electric characterizations were performed using a memristor characterizer device.

Data availability

The datasets used and/or analyzed during the current study available from the corresponding author on reasonable request.

Received: 4 January 2025; Accepted: 5 May 2025

References

1. Muscat, A. et al. Principles, drivers and opportunities of a circular bioeconomy. *Nat. Food* **2**, 561–566 (2021).
2. Sherwood, J. The significance of biomass in a circular economy. *Bioresour Technol.* **300**, 122755 (2020).
3. Chen, C. C., Dai, L., Ma, L. & Guo, R. T. Enzymatic degradation of plant biomass and synthetic polymers. *Nat. Rev. Chem.* **4**, 114–126 (2020).
4. Liu, Z. et al. Transforming biorefinery designs with 'Plug-In processes of lignin'to enable economic waste valorization. *Nat. Commun.* **12**, 3912 (2021).
5. Tuck, C. O., Pérez, E., Horváth, I. T., Sheldon, R. A. & Poliakoff, M. Valorization of biomass: Deriving more value from waste. *Science* **337**, 695–699 (2012).
6. Mujtaba, M. et al. Lignocellulosic biomass from agricultural waste to the circular economy: A review with focus on biofuels, biocomposites and bioplastics. *J. Clean. Prod.* **402**, 136815 (2023).
7. Zahid, A., Muhammad, G. & Muhammad, I. Agro-industrial lignocellulosic biomass a key to unlock the future bio-energy: A brief review. *J. Radiat. Res. Appl. Sci.* **7**, 163–173 (2014).
8. Tao, J. et al. Natural variability and antioxidant properties of commercially cultivated Switchgrass extractives. *Ind. Crops Prod.* **138**, 111474 (2019).
9. N'Guessan, J. L. L., Niamké, B. F., Yao, N. G. J. C. & Amusant, N. Wood extractives: Main families, functional properties, fields of application and interest of wood waste. *For. Prod. J.* **73**, 194–208 (2023).
10. Amrouk, E. M., Palmeri, F. & Magrini, E. Global coffee market and recent price developments. Preprint at (2025). https://www.fao.org/markets-and-trade/commoditiesoverview/beverages/coffee/en
11. Pham, Y., Reardon-Smith, K., Mushtaq, S. & Cockfield, G. The impact of climate change and variability on coffee production: A systematic review. *Clim. Change* **156**, 609–630 (2019).
12. Patil, S., Vedashree, M. & Murthy, P. S. Phytochemical profile and antioxidant potential of coffee leaves influenced by green extraction techniques and in vitro bio-accessibility of its functional compounds. *J. Food Meas. Charact.* **16**, 2335–2346 (2022).
13. Patil, S., Vedashree, M. & Murthy, P. S. Valorization of coffee leaves as a potential agri-food resource: Bio-active compounds, applications and future prospective. *Planta* **255**, 67 (2022).
14. Chen, X. A. & Review on Coffee leaves: Phytochemicals, bioactivities and applications. *Crit. Rev. Food Sci. Nutr.* **59**, 1008–1025 (2019).
15. Sathishkumar, P., Gu, F. L., Zhan, O., Palvannan, T. & Yusoff, A. R. M. Flavonoids mediated 'green'nanomaterials: A novel nanomedicine system to treat various diseases–Current trends and future perspective. *Mater. Lett.* **210**, 26–30 (2018).
16. Ngamsuk, S., Huang, T. C. & Hsu, J. L. Determination of Phenolic Compounds, Procyanidins, and Antioxidant Activity in Processed *Coffea arabica L.* Leaves. *Foods* **8**, 389 (2019).
17. Zahra, Z., Habib, Z., Chung, S. & Badshah, M. A. Exposure route of TiO2 NPs from industrial applications to wastewater treatment and their impacts on the agro-environment. *Nanomaterials* **10**, 1469 (2020).
18. Hasan, S. A review on nanoparticles: Their synthesis and types. *Res. J. Recent. Sci.* **4**, 9–11 (2015).
19. Yaqoob, A. A. et al. Recent advances in metal decorated nanomaterials and their various biological applications: A review. *Front. Chem.* **8**, 1–23 (2020).
20. Habibullah, G., Viktorova, J. & Ruml, T. Current strategies for noble metal nanoparticle synthesis. *Nanoscale Res. Lett.* **16**, 47 (2021).
21. Gupta, R. & Xie, H. Nanoparticles in daily life: Applications, toxicity and regulations. *J. Environ. Pathol. Toxicol. Oncol.* **37**, 209–230 (2018).
22. Ying, S. et al. Green synthesis of nanoparticles: Current developments and limitations. *Environ. Technol. Innov.* **26**, 102336 (2022).
23. Joudeh, N. & Linke, D. Nanoparticle classification, physicochemical properties, characterization, and applications: A comprehensive review for biologists. *J. Nanobiotechnol.* **20**, 262 (2022).

24. Dutta, G. & Sugumaran, A. Bioengineered zinc oxide nanoparticles: Chemical, green, biological fabrication methods and its potential biomedical applications. *J. Drug Del. Sci. Tech.* **66**, 102853 (2021).
25. Kumari, S. C., Dhand, V. & Padma, P. N. Green synthesis of metallic nanoparticles: A review. *Nanomaterials* 259–281 (2021).
26. Mandal, A. K. et al. Current research on zinc oxide nanoparticles: Synthesis, characterization, and biomedical applications. *Nanomaterials* **12**, 3066 (2022).
27. Qi, K., Cheng, B., Yu, J. & Ho, W. Review on the improvement of the photocatalytic and antibacterial activities of ZnO. *J. Alloys Compd.* **727**, 792–820 (2017).
28. Riahi, S. et al. Bactericidal activity of ZnO nanoparticles against multidrug-resistant bacteria. *J. Mol. Liq*. **387**, 122596 (2023).
29. Dlamini, Z. et al. Resistive switching in CdTe/CdSe Core–Shell quantum Dots embedded Chitosan-Based memory devices. *J. Circuits Syst. Comput.* **31**, 1–16 (2022).
30. Russo, U., Cagli, C., Spiga, S., Cianci, E. & Ielmini, D. Impact of electrode materials on Resistive-Switching memory programming. *IEEE Electron. Device Lett.* **30**, 817–819 (2009).
31. Lu, Q. et al. Biological receptor-inspired flexible artificial synapse based on ionic dynamics. *Microsyst. Nanoeng*. **6**, 84 (2020).
32. Ahmed, T. Bio-inspired artificial synapses: Neuromorphic computing chip engineering with soft biomaterials. *Mem. Mater.* **6**, 100088 (2023).
33. Nowak, E., Chłopocka, E. & Szybowicz, M. ZnO and ZnO-Based materials as active layer in resistive Random-Access memory (RRAM). *Crystals* **13**, 416 (2023).
34. Dlamini, Z. W. et al. Conduction and resistive switching in dropcast CdTe/CdSe Core-Shell quantum Dots embedded Chitosan composite. *Iran. J. Sci. Technol. A* **46**, 709–716 (2022).
35. Vallabhapurapu, S. et al. Optical and resistive switching properties of Chitosan-aluminum-doped zinc oxide composite thin films for transparent resistive random access memory application. *J. Mater. Sci. : Mater. Electron.* **32**, 3556–3565 (2021).
36. Guilger-Casagrande, M. & de Lima, R. Synthesis of silver nanoparticles mediated by fungi: A review. *Front. Bioeng. Biotechnol.* **7**, 287 (2019).
37. Morkoç, H. & Özgür, Ü. *Zinc Oxide: Fundamentals, Materials and Device Technology*131–244 (ed. Wiley, 2008).
38. Jay Chithra, M., Sathya, M. & Pushpanathan, K. J. A. M. S. Effect of pH on crystal size and photoluminescence property of ZnO nanoparticles prepared by chemical precipitation method. *Acta Metall. Sin -Engl Lett.* **28**, 394–404 (2015).
39. Soto-Robles, C. A. et al. Study on the effect of the concentration of Hibiscus sabdariffa extract on the green synthesis of ZnO nanoparticles. *Results Phys.* **15**, 102807 (2019).
40. Parra, M. R. & Haque, F. Z. Aqueous chemical route synthesis and the effect of calcination temperature on the structural and optical properties of ZnO nanoparticles. *J. Mater. Res. Technol.* **3**, 363–369 (2014).
41. Erat, S. et al. Solution-Processable growth and characterization of Dandelion-like ZnO:B microflower structures. *Crystals* **12**, 11 (2022).
42. Fu, L. & Fu, Z. *Plectranthus amboinicus* leaf extract-assisted biosynthesis of ZnO nanoparticles and their photocatalytic activity. *Ceram. Int.* **41**, 2492–2496 (2015).
43. Klein, J. et al. Limitations of the Tauc plot method. *Adv. Funct. Mater.* **33**, 2304523 (2023).
44. Verma, L. M. et al. Phase controlled green synthesis of wurtzite (P 63 mc) ZnO nanoparticles: Interplay of green ligands with precursor anions, anisotropy and photocatalysis. *Nanoscale Adv.* **6**, 155–169 (2024).
45. Faisal, S. et al. Green synthesis of zinc oxide (ZnO) nanoparticles using aqueous fruit extracts of *Myristica fragrans*: Their characterizations and biological and environmental applications. *ACS Omega*. **6**, 9709–9722 (2021).
46. Narayana, A. et al. Green and low-cost synthesis of zinc oxide nanoparticles and their application in transistor-based carbon monoxide sensing. *RSC Adv.* **10**, 13532–13542 (2020).
47. Yu, H. Y., Chen, G. Y., Wang, Y. B. & Yao, J. M. A facile one-pot route for Preparing cellulose nanocrystal/zinc oxide nanohybrids with high antibacterial and photocatalytic activity. *Cellulose* **22**, 261–273 (2015).
48. Aldeen, T. S., Mohamed, H. E. A. & Maaza, M. ZnO nanoparticles prepared via a green synthesis approach: Physical properties, photocatalytic and antibacterial activity. *J. Phys. Chem. Solids* **160**, 110313 (2022).
49. Sedefoglu, N. Green synthesis of ZnO nanoparticles by *Myrtus communis* plant extract with investigation of effect of precursor, calcination temperature and study of photocatalytic performance. *Ceram. Int.* **50**, 9884–9895 (2024).
50. Hameed, H. et al. Green synthesis of zinc oxide (ZnO) nanoparticles from green algae and their assessment in various biological applications. *Micromachines* **14**, 928 (2023).
51. Falke, S. & Betzel, C. Dynamic Light Scattering (DLS). In Radiation in Bioanalysis: Spectroscopic Techniques and Theoretical Methods (eds. Pereira, A. S., Tavares, P. & Limao-Vieira, P.) 173–193 (Springer International Publishing), (2019).
52. Kordy, M. G. et al. Phyto-capped ag nanoparticles: Green synthesis, characterization, and catalytic and antioxidant activities. *Nanomaterials* **12**, 373 (2022).
53. Wang, Q., Mei, S., Manivel, P., Ma, H. & Chen, X. Zinc oxide nanoparticles synthesized using coffee leaf extract assisted with ultrasound as nanocarriers for mangiferin. *Curr. Res. Food Sci.* **5**, 868–877 (2022).
54. Sidhu, A. K., Verma, N. & Kaushal, P. Role of biogenic capping agents in the synthesis of metallic nanoparticles and evaluation of their therapeutic potential. *Front. Nanotechnol.* **3**, 801620 (2022).
55. Tsegaye, G., Kiflie, Z., Mekonnen, T. H. & Jida, M. Synthesis and characterization of coffee husk extract (CHE)-capped ZnO nanoparticles and their antimicrobial activity. *Biomass Convers. Biorefin* 1–13 (2023).
56. Mahalakshmi, S., Hema, N. & Vijaya, P. P. In vitro biocompatibility and antimicrobial activities of zinc oxide nanoparticles (ZnO NPs) prepared by chemical and green synthetic route a comparative study. *BioNanoScience* **10**, 112–121 (2020).
57. Matinise, N., Fuku, X. G., Kaviyarasu, K., Mayedwa, N. & Maaza, M. ZnO nanoparticles via *Moringa oleifera* green synthesis: Physical properties & mechanism of formation. *Appl. Surf. Sci.* **406**, 339–347 (2017).
58. Barzinjy, A. A. & Azeez, H. H. Green synthesis and characterization of zinc oxide nanoparticles using Eucalyptus globulus labill. Leaf extract and zinc nitrate hexahydrate salt. *SN Appl. Sci.* **2**, 991 (2020).
59. Liu, I. T., Hon, M. H. & Teoh, L. G. Structure and optical properties of CeO2 nanoparticles synthesized by precipitation. *J. Electron. Mater.* **42**, 2536–2541 (2013).
60. Al-Taweel, S. S. & Saud, H. R. New route for synthesis of pure anatase TiO2 nanoparticles via utrasound-assisted sol-gel method. *J. Chem. Pharm. Res.* **8**, 620–626 (2016).
61. Sharma, A., Karn, R. K. & Pandiyan, S. K. Synthesis of TiO2 nanoparticles by sol-gel method and their characterization. *J. Basic. Appl. Eng. Res.* **1**, 1–5 (2014).
62. Khedr, M. H., Omar, A. A. & Abdel-Moaty, S. A. Magnetic nanocomposites: Preparation and characterization of Co-ferrite nanoparticles. *Coll. Surf. A* **281**, 1–3 (2006).
63. Maro, C. A. G. et al. *Peumus boldus* used in the synthesis of ZnO semiconductor nanoparticles and their evaluation in organic contaminants. *Materials* **16**, 4344 (2023).
64. Galland, D. & Herve, A. ESR spectra of the zinc vacancy in ZnO. *Phys. Lett. A*. **33**, 1–2 (1970).
65. Taylor, A. L., Filipovich, G. & Lindeberg, G. K. Electron paramagnetic resonance associated with Zn vacancies in neutron-irradiated ZnO. *Solid State Commun.* **8**, 1359–1361 (1970).
66. Mahule, T. S., Srinivasu, V. V. & Das, J. Electron spin resonance study of Co-doped ZnO system: Spin-Canted magnetism and sintering effects. *J. Supercond Nov Magn.* **30**, 1377–1380 (2017).

67. Jin, S. E. & Jin, H. E. Antimicrobial activity of zinc oxide nano/microparticles and their combinations against pathogenic microorganisms for biomedical applications: From physicochemical characteristics to Pharmacological aspects. *Nanomaterials* **11**, 263 (2021).
68. Sirelkhatim, A. et al. Review on zinc oxide nanoparticles: Antibacterial activity and toxicity mechanism. *Nanomicro Lett.* **7**, 219–242 (2015).
69. Jiang, J., Pi, J. & Cai, J. The advancing of zinc oxide nanoparticles for biomedical applications. *Bioinorg. Chem. Appl.* **5**, 1062562 (2018).
70. Siddiqi, K. S., Husen, A. & Rao, R. A. K. A review on biosynthesis of silver nanoparticles and their biocidal properties. *J. Nanobiotechnol.* **16**, 16 (2018).
71. Guo, Y. et al. Multifunctional PtCuTe nanosheets with strong ROS scavenging and ROS-independent antibacterial properties promote diabetic wound healing. *Adv. Maters*. **36**, 2306292 (2024).
72. Lee, H. & Lee, D. G. Gold nanoparticles induce a reactive oxygen species-independent apoptotic pathway in Escherichia coli. *Colloids Surf., B*. **167**, 1–7 (2018).
73. Kadiyala, U., Turali-Emre, E. S., Bahng, J. H., Kotov, N. A. & Vanepps, J. S. Unexpected insights into antibacterial activity of zinc oxide nanoparticles against methicillin resistant *Staphylococcus aureus* (MRSA). *Nanoscale* **10**, 4927–4939 (2018).
74. Doğaroğlu, Z. G., Uysal, Y., çaylalı, Z. & Karakulak, D. S. Green nanotechnology advances: Green manufacturing of zinc nanoparticles, characterization, and foliar application on wheat and antibacterial characteristics using *Mentha spicata* (mint) and *Ocimum basilicum* (basil) leaf extracts. *Environ. Sci. Pollut Res. Int.* **30**, 60820–60837 (2023).
75. Rutherford, D. et al. Growth inhibition of gram-positive and gram-negative bacteria by zinc oxide Hedgehog particles. *Int. J. Nanomed.* **16**, 3541–3554 (2021).
76. Hossain, T. J. Methods for screening and evaluation of antimicrobial activity: A review of protocols, advantages, and limitations. *Eur. J. Microbiol. Immunol.* **14**, 97–115 (2024).
77. Chung, E. et al. Applied methods to assess the antimicrobial activity of metallic-based nanoparticles. *Bioengineering* **10**, 1259 (2023).
78. Emami-Karvani, Z. & Chehrazi, P. Antibacterial activity of ZnO nanoparticle on gram-positive and gram-negative bacteria. *Afr. J. Microbiol. Res.* **5**, 1368–1373 (2011).
79. Alekish, M., Ismail, Z. B., Albiss, B. & Nawasrah, S. In vitro antibacterial effects of zinc oxide nanoparticles on multiple drug-resistant strains of *Staphylococcus aureus* and *Escherichia coli*: An alternative approach for antibacterial therapy of mastitis in sheep. *Vet. World* **10**, 1428–1432 (2018).
80. Yusof, N. A. A., Zain, N. M. & Pauzi, N. Synthesis of ZnO nanoparticles with Chitosan as stabilizing agent and their antibacterial properties against Gram-positive and Gram-negative bacteria. *Int. J. Biol. Macromol.* **1**, 1132–1136 (2019).
81. Naila, Z. & Khalida, A. Morphology controlled synthesis of ZnO nanoparticles for in-vitro evaluation of antibacterial activity. *Trans. Nonferrous Met. Soc. China*. **30**, 1605–1614 (2020).
82. Raghupathi, K. R., Koodali, R. T. & Manna, A. C. Size-dependent bacterial growth Inhibition and mechanism of antibacterial activity of zinc oxide nanoparticles. *Langmuir* **7**, 4020–4028 (2011).
83. Mirhosseini, M. & Firouzabadi, F. B. Antibacterial activity of zinc oxide nanoparticle suspensions on food-borne pathogens. *Int. J. Dairy. Technol.* **66**, 291–295 (2013).
84. Babayevska, N. et al. ZnO size and shape effect on antibacterial activity and cytotoxicity profile. *Sci. Rep.* **12**, 8148 (2022).
85. Singh, K., Nancy, Bhattu, M., Singh, G., Mubarak, N. M. & Singh, J. Light-absorption-driven photocatalysis and antimicrobial potential of PVP-capped zinc oxide nanoparticles. *Sci. Rep.* **13**, 13886 (2023).
86. Azmina, M. S. et al. Enhanced photocatalytic activity of ZnO nanoparticles grown on porous silica microparticles. *Appl. Nanosci.* **7**, 885–892 (2017).
87. Venkatesan, S. et al. Methylene blue dye degradation potential of zinc oxide nanoparticles bioreduced using *Solanum trilobatum* leaf extract. *Results Chem.* **4**, 100637 (2022).
88. Tang, S. et al. Enhanced photocatalytic performance of BiVO4 for degradation of methylene blue under LED visible light irradiation assisted by peroxymonosulfate. *Int. J. Electrochem. Sci.* **15**, 2470–2480 (2020).
89. Nisar, A. et al. Kinetic modeling of ZnO-rGO catalyzed degradation of methylene blue. *Int. J. Chem. Kinet.* **52**, 645–654 (2020).
90. Hkiri, K., Mohamed, H. E. A., Ghotekar, S. & Maaza, M. Green synthesis of cerium oxide nanoparticles using portulaca oleracea extract: Photocatalytic activities. *Inorg. Chem. Commun.* **162**, 112243 (2024).
91. Vinayagam, R. et al. Green synthesized Cobalt oxide nanoparticles with photocatalytic activity towards dye removal. *Environ. Res.* **216**, 114766 (2023).
92. Bahsis, L. et al. Copper oxide nanoparticles-decorated cellulose acetate: Eco-friendly catalysts for reduction of toxic organic dyes in aqueous media. *Int. J. Biol. Macromol.* **284**, 137982 (2025).
93. Ablouh, E. H. et al. Eco-friendly Cu_2O/Cu nanoparticles encapsulated in cellulose acetate: A sustainable catalyst for 4-nitrophenol reduction and antibacterial applications. *J. Environ. Chem. Eng.* **13**, 115077 (2025).
94. Benhadria, E. et al. Cellulose Acetate-Stabilized Cu2O nanoparticles for enhanced catalytic reduction of organic pollutants. *J. Inorg. Organomet. Polym.* (2024).
95. Zelekew, O. A., Haitosa, H. H., Chen, X. & Wu, Y. N. Recent progress on plant extract-mediated biosynthesis of ZnO-based nanocatalysts for environmental remediation: Challenges and future outlooks. *Adv. Colloid Interface Sci.* **317**, 102931 (2023).
96. Nayak, S., Goveas, L. C., Selvaraj, R., Mutalik, S. & Sajankila, S. P. Use of cyclea peltata mediated gold nanospheres for adsorptive degradation of Methyl green dye. *Bioresour Technol.* **20**, 10126 (2022).
97. Nayak, S., Goveas, L. C. & Sajankila, S. P. Exploring the efficacy of Pongamia pinnata-induced silver nanoflowers for efficient adsorptive degradation of malachite green dye. *Biotech. Sustain.* **1**, 17 (2024).
98. Elemike, E. E., Onwudiwe, D. C. & Mbonu, J. I. Green synthesis, structural characterization and photocatalytic activities of Chitosan-ZnO Nano-composite. *J. Inorg. Organomet. Polym. Mater.* **31**, 3356–3367 (2021).
99. Kumar, R., Ranwa, S. & Kumar, G. Biodegradable flexible substrate based on Chitosan/PVP blend polymer for disposable electronics device applications. *J. Phys. Chem. B* **124**, 149–155 (2019).
100. Gurylev, V. & Perng, T. P. Defect engineering of ZnO: Review on oxygen and zinc vacancies. *J. Eur. Ceram. Soc.* **41**, 4977–4996 (2021).
101. Vallabhapurapu, S. et al. Resistive switching in reduced graphene oxide incorporated Polyvinyl alcohol films. *Mater. Today Proc.* **9**, 615–620 (2019).
102. Deb, R. et al. ZnO Nanoparticle-Induced performance enhancement of a Coumarin-Based nonvolatile memory device. *ACS Appl. Eng. Mater.* **2**, 1141–1152 (2024).
103. Simanjuntak, F. M., Ohno, T., Minami, K. & Samukawa, S. Transparent ZnO resistive switching memory fabricated by neutral oxygen beam treatment. *Jpn J. Appl.* **61**, SM1010 (2022).
104. Patil, S. R. et al. Solution-processable ZnO thin film memristive device for resistive random access memory application. *Electronics* **7**, 445 (2018).
105. Xu, Z., Yu, L., Xu, X., Miao, J. & Jiang, Y. Effect of oxide/oxide interface on Polarity dependent resistive switching behavior in ZnO/ZrO2 heterostructures. *Appl. Phys. Lett.* **104**, 192903 (2014).
106. Ismail, M. et al. Effect of bilayer ceo 2 – x/ZnO and ZnO/CeO 2 – x heterostructures and electroforming Polarity on switching properties of non-volatile memory. *Nanoscale Res. Lett.* **13**, 1–10 (2018).
107. Vallabhapurapu, S. et al. Resistive switching behaviour in PMMA/Al: ZnO composite films. *Acta Phys. Pol.* **134**, 68–70 (2018).

108. Monshi, A., Foroughi, M. R. & Monshi, M. R. Modified Scherrer equation to estimate more accurately nano-crystallite size using XRD. *WJNSE*. 2, 154–160 (2012).
109. Costa, P., Gomes, A. T. P. C., Braz, M., Pereira, C. & Almeida, A. Application of the resazurin cell viability assay to monitor Escherichia coli and Salmonella Typhimurium inactivation mediated by phages. *Antibiotics* **10** (2021).
110. Samaniego, L. V. B. et al. Thermothelomyces thermophilus exo- and endo-glucanases as tools for pathogenic E. coli biofilm. *Sci. Rep.* **14**, 22576 (2024).

Acknowledgements

This work was supported by the Fundação de Amparo à Pesquisa do Estado de São Paulo (FAPESP, grants #2021/08780-1 and 2024/00533-3 to IP), by the Conselho Nacional de Desenvolvimento Científico e Tecnológico (CNPq, grants #306852/2021-7 and 440180/2022-8 to IP). Partial support from BRICS-NRF project Grant no. 150501, Unrated NRF grant Reference/Grant Number: SRUG2204305453 and DRSP grant from UNISA are acknowledged. ZWD wants to acknowledge the CUT-UFS Seed grant for MIT project, and the NRF Africa University Twinning project (grant number AUTP240325210690).

Author contributions

V.O.A.P., F.T.T. and I.P. designed the experiments; V.O.A.P. and A.J.B. synthesized the NPs, V.O.A.P., A.J.B., R.R.L., J.F.P., M.I.B.B., V.S.V. and T.S.M. conducted characterization of the NPs; A.N.G.D. and C.R.F. performed antimicrobial studies, Z.W.D., S.V., V.S.V. and B.B.M. contributed with bioReRAM assembly and characterizations; R.R.L., A.J.B. and M.I.B.B. conducted photodegradation studies; V.O.A.P., F.T.T., B.Q.M., V.S.V., Z.W.D., R.R.L., M.I.B.B. and I.P. wrote the manuscript with the input from all the other authors; I.P., V.S.V., F.T.T. and B.Q.M. secured funding and I.P. and V.S.V., supervised the project. All authors reviewed the manuscript.

Declarations

Competing interests

The authors declare no competing interests.

Additional information

Supplementary Information The online version contains supplementary material available at https://doi.org/10.1038/s41598-025-01260-3.

Correspondence and requests for materials should be addressed to F.T.T. or I.P.

Reprints and permissions information is available at www.nature.com/reprints.